Proceedings of the 21st ICSMGE, Vienna, Austria, 14 – 19 June 2026. Pistrol, Adam & Schweiger (eds.)
Published by: ÖGG, Austrian Society for Geomechanics, Salzburg, Austria, ISBN 978-3-9503898-4-5
https://doi.org/10.53243/ICSMGE2026-990

Development of a Scalable Landslide Early Warning System Using Geospatial and Meteorological Data Fusion

Kunal Gupta, Neelima Satyam Devarakonda
Department of Civil Engineering, Indian Institute of Technology Indore, India, kunalgupta.academics@gmail.com

ABSTRACT: This research develops and validates a dynamic landslide early warning system for the Chamoli district in Uttarakhand, India, significantly improving prediction accuracy and practical usability. The foundation is a slope unit–based susceptibility map created with an optimised Random Forest model achieving an AUC-ROC of 0.936. To address the temporal shortcomings of static susceptibility maps, the system incorporates locally tailored SIGMA rainfall thresholds that reflect the region's specific conditions. This combined approach enables spatiotemporal hazard detection by issuing high-level alerts only when both susceptibility and rainfall exceed critical levels simultaneously. Alerts are categorised into four levels: Green (No Alert), Yellow (Ordinary), Orange (Moderate), and Red (High) to indicate increasing landslide risk. Validation with 2020–2021 data showed perfect sensitivity and negative predictive power, accurately forecasting all 44 recorded landslides while avoiding false alarms during stable periods. Further operational testing with 2022–2024 data confirmed that 92.7% of landslides happened during Red alerts, with none during Green or Yellow phases. Using slope units instead of pixels prevents fragmented mapping outputs, enhancing map clarity and supporting focused mitigation, monitoring, and emergency response. By providing timely and location-specific warnings, this system turns static hazard data into actionable insights, reduces false alarms, and facilitates efficient resource allocation during critical events. The framework offers a reliable, scalable solution that advances landslide risk management beyond traditional methods.

KEYWORDS: Landslide, Early Warning System, Rainfall Thresholds, Susceptibility Mapping, Random Forest

1 INTRODUCTION

Landslides are among the most damaging natural hazards, with rainfall-triggered events causing over 5,000 deaths and $20 billion in annual global losses (Petley, 2012). Climate change has intensified extreme rainfall, especially in mountains, worsening slope instability. In Asia, such losses have increased by 147% since 2001 (Haque et al., 2019). The Himalayas are particularly at risk due to tectonic uplift, monsoons, and glacial retreat (Froude and Petley, 2018). Despite supporting 1.9 billion people, many Himalayan regions like Chamoli, India, lack operational Landslide Early Warning Systems (LEWS) (Wester et al., 2020).

Physically based models like TRIGRS and FSLAM require detailed geotechnical data, often missing in such terrains (Baum, Savage and Godt, 2008). Simpler empirical rainfall thresholds are easier to apply but prone to false alarms (Abraham et al., 2020b; 2020a). Static susceptibility maps, even with machine learning, fail to predict timing (Mittal, Gupta and Satyam, 2024). Hybrid models combining susceptibility and rainfall thresholds address both spatial and temporal aspects more effectively (Segoni et al., 2018).

However, many LEWS still rely on rigid, grid-based maps, limiting their precision (Reichenbach et al., 2018). Slope Units (SUs) offer a better alternative by aligning with natural terrain features (Alvioli et al., 2016), yet no hybrid system has fully integrated SU-based mapping with dynamic thresholds. Chamoli, with its complex geology and frequent rainfall and earthquakes, exemplifies this gap, lacking both SU-based LSM and calibrated thresholds, leaving current warnings inadequate.

This study introduces the first hybrid LEWS that combines SU-based susceptibility with dynamically calibrated rainfall thresholds. Unlike conventional systems, it accounts for both spatial instability and evolving meteorological triggers. Susceptibility is mapped using geomorphologically meaningful SUs, avoiding pixel-level noise and enabling focused monitoring. The Random Forest (RF) model is optimised via hyperparameter tuning, built from extensive landslide records and conditioning factors. A dual-timescale rainfall thresholding method captures both rapid shallow failures and deeper, delayed landslides.

The system dynamically updates warnings by pairing static susceptibility with real-time rainfall, activating alerts even in low-risk SUs if rainfall exceeds σ thresholds. This adaptive logic captures transient hazards and minimises false alarms. Validation shows high spatial-temporal accuracy, with landslides aligning with high-alert periods. SU-based modelling also improves computational efficiency, making the system scalable for data-scarce, high-risk regions like Chamoli.

2 STUDY AREA

Chamoli district, located in Uttarakhand, India (Figure 1), is highly prone to rainfall-induced landslides due to its steep topography, active tectonic setting, and intense seasonal precipitation. Covering around 7,700 km², the region spans elevations from 660 m to over 7,100 m, making it geomorphologically diverse and unstable.

Geologically, Chamoli lies within the tectonically active Himalayas and is divided into two main zones. The northern zone contains high-grade metamorphic rocks like schists and gneisses, while the southern zone features sedimentary and low-grade metamorphic formations such as limestone and phyllites. Major fault lines like the Main Central Thrust (MCT) and Main Boundary Fault (MBF) run through the district, contributing to frequent slope instability.

The region's landscape is shaped by towering peaks, deep valleys, and glacial activity. Rivers such as the Alaknanda, Pindar, and Dhauli Ganga, fed by glacial melt and monsoon rains, play a key role in triggering slope failures. The hydrology is dominated by steep river systems that cause erosion and slope saturation during peak flows.

Chamoli is also part of a seismically active zone, with earthquakes regularly destabilising already fragile slopes. Combined with high rainfall, over 1,200 mm annually, mostly during July–September, these factors make the area especially susceptible to landslides, both shallow and deep-seated (GSI, 2024).

The district holds major socio-economic importance, hosting tourist and pilgrimage sites like Badrinath. However, infrastructure developments and high human activity further increase environmental stress. Past disasters, including the 2013 flash floods and the 2021 Ronti avalanche, have caused massive destruction. The most recent 2025 avalanche near Mana village again underscored the urgent need for robust, spatially adaptive LEWS in Chamoli.

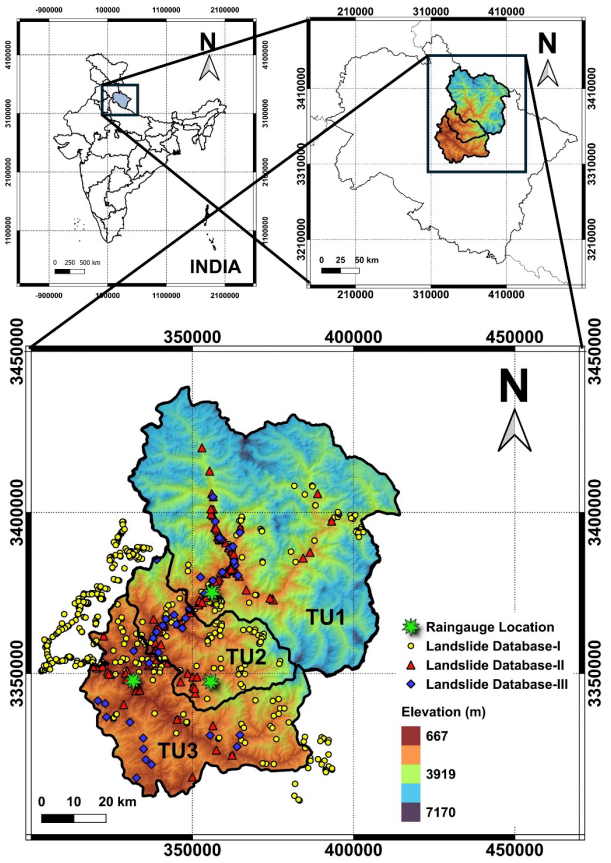

Figure 1. Study area location shown as: (a) India, (b) Uttarakhand state, (c) Chamoli district.

3 METHODOLOGY

3.1 *Data Acquisition and Curation*

To build a comprehensive landslide dataset for Chamoli district, multiple sources were combined, including field surveys, satellite imagery, government reports, and records from agencies such as the Border Roads Organisation (BRO), the National Highways Authority of India (NHAI), and the Geological Survey of India (GSI). Initially, 244 landslides were identified within Chamoli district. To improve regional coverage, a 30 km buffer was added around the district boundary, resulting in a final inventory of 518 landslide events. This expanded inventory, referred to as Landslide Database-I, included georeferenced landslide points and polygons, along with metadata like date of occurrence, landslide type, and triggers. From this, a subset of 121 dated landslides between 2006 and 2019 was used to develop rainfall thresholds, while 44 events from 2020–2021 were reserved for independent validation (Landslide Database-II). An additional set of 41 events from 2022–2024 was excluded from model development to test the real-time performance of the early warning system (Landslide Database-III).

To understand the factors contributing to landslides, 14 causative variables were selected to cover physical, geological, hydrological, climatic, and human influences on slope stability. These factors were gathered from satellite data, digital elevation models (DEM), geological surveys, and open databases. Key topographic features like slope and aspect were derived from a high-resolution DEM from ALOSPALSAR, (2015). Hydrological indicators included the Topographic Wetness Index (TWI) and Stream Power Index (SPI), calculated using flow accumulation data from the D8 algorithm. Vegetation cover was represented by the Normalised Difference Vegetation Index (NDVI). Geological and geomorphological information, such as rock types, landforms, and distances to structural features like lineaments, came from the Geological Survey of India (GSI, 2024). Human impacts were captured through proximity to roads, while seismic activity was represented using the Peak Ground Acceleration (PGA) spatial map obtained from (Gupta and Satyam, 2022), based on regional probabilistic seismic hazard models. Mean annual precipitation data, representing long-term rainfall trends, were obtained from the India Meteorological Department (IMD, 2025) and used to account for climatic influence.

All data layers were standardised to a 12.5 m spatial resolution using GIS techniques. Slope and aspect were calculated in QGIS, with aspect values grouped into eight main compass directions to reduce noise while preserving meaningful orientation patterns important for landslides. The SPI values were log-transformed to normalise their distribution for analysis. The geological map included seven formations with distinct rock types and properties. These formations ranged from Proterozoic units like the Yamunotri Formation (gneiss, schist, quartzite) to Mesoproterozoic groups such as the Berinag-Chamoli-Nagnithank Formation (schists, metavolcanics). Other formations included quartz mica schist and marble prone to karstification, and charnockite and granulite rocks forming resistant ridges but vulnerable to seismic fracturing. The alluvial deposits along rivers, consisting of unconsolidated sediments, were also mapped due to their susceptibility to liquefaction during earthquakes. Geological vector maps at a 1:50,000 scale from GSI (2024) data were converted to raster format with filtering to reduce pixel errors. This comprehensive set of causative factors formed the basis for assessing landslide susceptibility in the study area.

3.2 *Landslide Susceptibility Mapping*

Landslide susceptibility was modelled using SUs, which were delineated using SUMak, a tool that applies watershed-based segmentation principles from TauDEM and GRASS GIS. This approach ensures each unit aligns with natural drainage and slope patterns, helping to reduce mapping errors. A 12.5 m DEM was used to generate 6,566 SUs in the Chamoli district, optimised to reflect hillslope-scale processes. These units served as the spatial basis for modelling.

For model training, spatial data were extracted around 518 landslide initiation points verified through field surveys and satellite interpretation. An equal number of non-landslide points were selected from stable areas using stratified random sampling, avoiding extreme slopes and recent disturbances. Environmental variables were extracted for each point from all raster layers, creating a dataset of 1,036 entries with 17 attributes. All layers were aligned to a common projection and resolution.

Before model training, multicollinearity among variables was checked using correlation matrices and Variance Inflation Factors (VIF). Highly correlated variables were removed or transformed to ensure model reliability. An RF classifier was used for modelling due to its robustness and ability to handle nonlinear relationships and high-dimensional data. The dataset was split into 80% for training and 20% for testing. During training, hyperparameter tuning was performed using 10-fold cross-validation and grid search to identify the optimal number of trees, tree depth, and minimum samples per split.

The model's performance was evaluated using metrics such as AUC-ROC, accuracy, precision, recall, and F1-score. After validation, the trained RF model was applied to all SUs. Mean values of each causative factor within each SU were calculated to maintain internal consistency and reduce noise. The model output was a continuous susceptibility score

between 0 and 1 for each SU, which was categorised into four levels: Low, Moderate, High, and Very High susceptibility.

3.3 *SIGMA Thresholding Framework*

To support rainfall threshold estimation amid sparse rain gauge coverage, Chamoli district was reorganised from six administrative sub-districts into three territorial units (TUs). TU1 covers Joshimath, TU2 corresponds to Chamoli, and TU3 merges Karnaprayag, Pokhari, Gairsain, and Tharali. This consolidation balanced hydrological similarity with the limited availability of continuous rainfall data, a method consistent with earlier threshold-based landslide research (Lagomarsino et al., 2015; Abraham et al., 2021).

One automated rain gauge per TU was selected based on two main criteria: uninterrupted data from 2006 to 2024 and elevation similarity to landslide-prone zones. Though this approach introduces spatial generalisation, it reflects the practical constraints of Himalayan terrain, where dense instrumentation is rare (Vishwakarma et al., 2022).

Daily rainfall from 2006 to 2019 was used to derive σ thresholds, which were validated using 2020–2021 landslide records. TU2 received the highest cumulative rainfall, followed by TU3 and then TU1. TU3 also showed the highest interannual variability, while TU1 and TU2 exhibited more stable year-to-year trends. These differences highlight the district's diverse microclimates, shaped by topography and geographic orientation.

The SIGMA model, developed by Martelloni et al., (2012), is a regional LEWS originally designed for the Emilia-Romagna region in Italy. It is based on the idea that extreme rainfall, when evaluated in relation to long-term variability, can act as a reliable indicator of impending landslides. This is operationalised by defining rainfall thresholds as multiples of the standard deviation (σ) derived from historical rainfall records. These σ-thresholds mark deviations from normal conditions and help identify potentially dangerous rainfall episodes. Daily rainfall data from 2006 to 2019 are processed using a moving-window approach that constructs cumulative rainfall distributions over time windows ranging from 1 to 365 days. For each duration, cumulative rainfall is computed on a rolling basis for every rain gauge station, producing a detailed location-specific rainfall database.

Short-duration rainfall windows usually show skewed or lognormal-like distributions, while longer durations tend toward Gaussian behaviour. However, since actual distributions rarely conform to ideal statistical models, a quantile transformation is applied. This maps the empirical cumulative rainfall values to a standard Gaussian distribution, allowing non-exceedance probabilities to be assigned. Each rainfall value z_k is ranked, and its plotting position P_k is computed. Using the inverse Gaussian cumulative function G^{-1} , the standardised value y is obtained. This value represents how many standard deviations the rainfall lies from the mean, enabling the conversion of rainfall magnitudes into σ-space. This transformation is reversible: once a σ-threshold is chosen, the corresponding exceedance probability is retrieved from the Gaussian distribution and mapped back to real rainfall values. Repeating this across all durations from 1 to 365 days results in a family of σ-threshold curves, which describe rainfall amounts linked to various levels of exceedance probability (Lagomarsino et al., 2015). These curves, illustrated for up to 100-day durations at the TU1 reference station (Figure 2), form the statistical foundation of the SIGMA model.

For this study, the SIGMA concept was adapted and calibrated to suit the Chamoli district by developing a dual time-window threshold system. This localised system enables real-time hazard evaluation based on comparisons between recent rainfall data and σ-thresholds that reflect local rainfall climatology. Because shallow and deep-seated landslides respond to different hydrological mechanisms and timescales, the algorithm evaluates each type separately. Shallow landslides, often triggered by rapid surface saturation, are assessed using rainfall accumulated over the past 1, 2, and 3 days, including the current day:

$$C_{1-3}(t) = \sum_{i=1}^{n} \mathrm{P(t+1-i)},\ for\ n = 1, 2, 3 \quad (1)$$

Here, P(t) is the rainfall on day t. Each calculated value $C_n(t)$ is checked against its corresponding σ-threshold $S_n\ (\Delta)$, where Δ can take values such as 0.1σ, 0.5σ, 1σ, and 1.5σ. Exceeding the highest threshold for any duration triggers a high alert, indicating likely shallow slope failures.

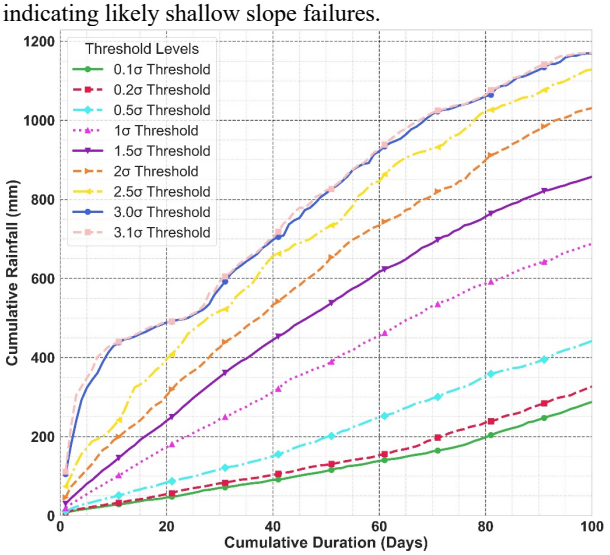

Figure 2. Illustration of σ curves representing cumulative rainfall durations up to 100 days at the TU1 reference rain gauge, based on data collected between 2006 and 2019.

For deep-seated landslides, where pore pressure builds up over longer periods, a seasonally adaptive accumulation approach is used. Cumulative rainfall is calculated starting from the fourth day before the current day, and the window length $D(t)$ varies by season. From November 1 to April 30, this duration increases linearly to reflect the accumulation of snow and delayed water infiltration, reaching up to 245 days:

$$S(t) = min(63 + (t - Nov\ 1),\ 245),\ t \in [Nov\ 1,\ Apr\ 30] \quad (2)$$

This default seasonal window $S(t)$ is then adjusted based on recent short-term rainfall. If three or more wet days (≥1 mm) occur in the past five days, the full 245-day window is applied. If there are four or more dry days, a shorter 30-day window is used. Otherwise, the seasonal default is maintained:

$$D(t) = \begin{cases} 245,\ if\ R_{wet}(t) \geq 3 \\ 30,\ \ \ \ \ if\ R_{dry}(t) \geq 4 \\ S(t),\ otherwise \end{cases} \quad (3)$$

Using this adaptive duration, cumulative rainfall is then calculated by excluding the last three days to avoid overlapping with the shallow landslide alert window:

$$C_{4-D(t)}(t) = \sum_{i=1}^{D(t)-3} \mathrm{P(t-2-i)} \quad (4)$$

The accumulated rainfall is compared against σ-thresholds that indicate ordinary, moderate, and high exceedance levels. If no shallow landslide alert is active but moderate or ordinary thresholds are exceeded for deep-seated landslides, corresponding alerts (yellow or orange) are issued. In the absence of threshold violations, the day is marked as green.

This four-colour classification: green (no alert), yellow (ordinary), orange (moderate), and red (high), helps distinguish between rapid and slow-onset hazard scenarios across the district.

The calibration of σ-thresholds for both landslide types is based on a data-driven optimisation process. Using a detailed landslide inventory, the algorithm tests whether rainfall prior to known events crossed any σ-thresholds. Initial threshold values are iteratively adjusted in steps of 0.05σ to minimise false positives, cases where thresholds were exceeded but no landslide occurred while preserving the number of true positives. This optimisation ends when no further reduction in false positives can be achieved without sacrificing true event detection.

3.4 *Coupling Susceptibility Mapping with Rainfall Thresholds*

To develop a spatially adaptive LEWS for Chamoli district, this study integrates a slope-unit-based susceptibility map with dynamic rainfall thresholds from the SIGMA model. Each SU is assigned a continuous susceptibility score between 0 and 1, later discretised into four classes: low (S0: 0–0.25), medium (S1: 0.25–0.5), high (S2: 0.5–0.75), and very high (S3: 0.75–1.0), capturing terrain variability. Independently, the SIGMA model assesses rainfall criticality using short- and long-term cumulative precipitation, with the latter determined by a seasonally adaptive duration $D(t)$. Rainfall totals are compared against σ-based probabilistic thresholds to assign each SU a rainfall criticality level: C0 (no exceedance), C1 (ordinary), C2 (moderate), or C3 (high). These rainfall levels $C_k \in \{0, 1, 2, 3\}$ are then combined with the susceptibility class $S_j \in \{0, 1, 2, 3\}$ for each SU using a graded early warning logic:

$$A_{ij} = C_k + S_j \tag{5}$$

This cumulative score defines the final alert level:

$$Alert\ level = \begin{cases} \text{Green (No Alert)} & \text{if } A_{ij} < 3 \\ \text{Yellow (Ordinary)} & \text{if } 3 \le A_{ij} < 4 \\ \text{Orange (Moderate)} & \text{if } 4 \le A_{ij} < 5 \\ \text{Red (High)} & \text{if } A_{ij} \ge 5 \end{cases} \tag{6}$$

This approach allows the system to respond proportionally to both hazard and vulnerability, for example, moderate rainfall over highly susceptible terrain can still trigger a red alert, while resistant areas may remain in green even under intense rainfall. The rainfall criticality is updated daily, while susceptibility remains static, enabling real-time, colour-coded GIS alerts that adapt to both spatial and temporal changes. This method enhances both accuracy and operational value, minimising false alarms while remaining sensitive to high-risk zones across Chamoli's diverse geomorphology.

4 RESULTS AND VALIDATION

4.1 *Landslide Susceptibility Assessment Using Slope Units*

The multicollinearity assessment examined the relationships among landslide causative factors using a correlation matrix and VIF analysis (Figure 3). Geomorphology correlated positively with slope and Log(SPI) but negatively with TWI, while TWI and slope showed a strong inverse relationship, reflecting the trade-off between wetness and steepness. NDVI was negatively related to elevation and distance from streams, with elevation positively correlated with distance to roads and streams but negatively with rainfall, highlighting orographic effects. PGA and rainfall correlated positively with NDVI. Variables with very high VIFs (above 40), such as TWI, slope, PGA, and Log(SPI), were excluded to avoid redundancy. Elevation and rainfall showed moderate collinearity but were retained after transformation. Elevation was binned into three classes to reduce collinearity while preserving trends, and rainfall was normalised by elevation to create a relative wetness index. These steps ensured independent and meaningful predictors across geomorphological, hydrological, geological, vegetative, and anthropogenic factors, improving model stability and scientific validity.

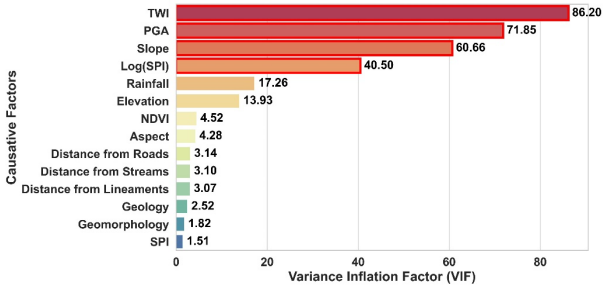

Figure 3. Variance Inflation Factor (VIF) analysis identifying the four key variables (marked with red rectangles) removed because of significant multicollinearity.

The RF model showed strong predictive performance with an AUC of 0.931, indicating an excellent ability to distinguish landslide-prone from stable areas (Figure 4(a)). Training accuracy was 0.986, while testing accuracy was 0.844, showing good generalisation. Precision was 0.821, minimising false alarms, and recall was 0.909, capturing most landslide events. The F1 score of 0.863 demonstrated balanced precision and recall. Cross-validation using the k-fold method confirmed consistent performance, with an average accuracy of 81.8%.

The SU-based landslide susceptibility map showed spatial variation in the study area, with "High" and "Very High" susceptibility classes together covering about 48.4% of SUs (Figure 5 (a)). These areas have elevated landslide risk and should be prioritised for monitoring and mitigation. The "Moderate" class covered 20.04%, while "Low" susceptibility areas accounted for 31.56%, indicating lower landslide likelihood. This distribution reflects the varied terrain and hazard potential across the region.

4.2 *SIGMA Rainfall Thresholds*

Calibration of σ thresholds was performed individually for each TU to account for local geological and hydrological variations by selecting the most appropriate subset of the original σ curves. This led to distinct optimised thresholds for each TU. For instance, in TU1, the ordinary alert threshold was adjusted from 0.1 to 0.2, the moderate alert remained at 1.0, and the high alert increased slightly from 1.4 to 1.6. TU2 showed a more pronounced change, with the ordinary alert threshold rising from 0.1 to 0.75, the moderate alert increasing from 1.0 to 1.55, and the high alert moving from 1.4 to 1.7, reflecting its low-permeability clay-rich bedrock that demands greater rainfall to trigger landslides. In TU3, the ordinary alert was optimised to 0.5 (from 0.1), the moderate alert to 1.3 (from 1.0), while the high alert threshold remained unchanged at 1.4.

Validation using landslide and rainfall data from 2020–2021 demonstrated that the SIGMA model achieved 100% sensitivity across all TUs by correctly predicting all 44 recorded landslides (27 in TU1, 6 in TU2, and 11 in TU3). Although the model generated varying numbers of false positives (such as 190 ordinary, 56 moderate, and 148 high alerts without observed landslides in TU1), the number of landslide events missed by the model (false negatives) was zero for all TUs, which is common in safety-prioritised early warning systems where missing events are costly.

To evaluate its predictive ability, several statistical metrics were calculated for each TU, as summarised in Table 1. Specificity ranged from 44% in TU1 to 66% in TU2, indicating

that many safe days still triggered alerts. This is reflected in the high false positive rate across all TUs. The positive predictive power (PPP) was low (between 2.4% and 6.2%), meaning only a small number of alerts corresponded to actual landslides, which is common in early warning systems designed to avoid missing any events.

Table 1. Performance metrics of the SIGMA model across Territorial Units (TUs)

Metric	TU1	TU2	TU3
Efficiency	0.461	0.6662	0.6088
Misclassification Rate	0.539	0.3338	0.3912
Odds Ratio	0.8553	1.9959	1.5559
Positive Predictive Power	0.0619	0.024	0.037
Negative Predictive Power	1	1	1
Sensitivity (Recall)	1	1	1
Specificity	0.4411	0.6634	0.6028
False Positive Rate	0.5589	0.3366	0.3972
False Negative Rate	0	0	0
Likelihood Ratio	1.7893	2.9713	2.5175

Despite frequent false alarms, the model showed perfect negative predictive power (100%) in all TUs, meaning no landslides occurred on days without alerts, offering high confidence during stable periods. Overall efficiency varied, from about 46% in TU1 to nearly 67% in TU2, with TU3 in between. This variation likely reflects differences in terrain, rainfall, and landslide mechanisms. As shown in Table 1, misclassification rates were higher in units with lower efficiency.

4.3 *Validation of the Dynamic Landslide Early Warning System in Operation*

The operational reliability and real-time prediction capability of the integrated dynamic LEWS were thoroughly tested using Landslide Database-III, which was kept entirely separate from the data used for developing the σ thresholds. This ensured an unbiased evaluation that reflects the system's true performance under current conditions.

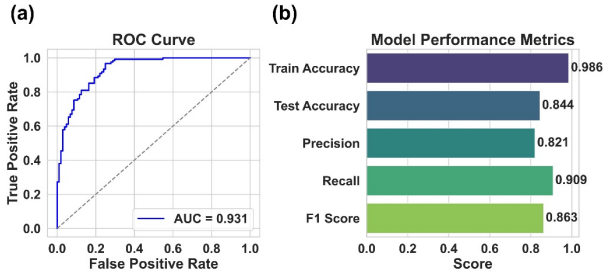

Figure 4. Summary of landslide susceptibility model evaluation: (a) ROC curve; (b) Performance metrics of the model.

During the validation period, TU1 recorded 14 landslides, with the majority occurring in Low and Moderate susceptibility zones; specifically, 8 landslides in Low and 5 in Moderate susceptibility, and only 1 in High susceptibility. TU2 had a more even spread with 2 landslides in Low, 3 in Moderate, and 8 in High susceptibility classes. TU3 also saw most landslides in Low and Moderate categories, with 5 and 8, respectively, and just 1 in High. Notably, no landslides were recorded in the Very High susceptibility class across all units.

Regarding alert performance, the system showed strong predictive skill. No landslides occurred on days classified under Green or Yellow alerts in any TU. In TU1, out of 14 landslides, 13 happened during Red alert days and one during an Orange alert day. TU2 experienced all 13 landslides during Red alert days. In TU3, 12 out of 14 landslides occurred on Red alert days, and 2 on Orange. Overall, 38 of the 41 landslides (approximately 92.7%) were correctly predicted during Red alerts, with all events captured within either Orange or Red alert periods. The number of days under each alert level varied, with Red alerts active for a substantial portion of the time—for instance, TU1 had 242 Red alert days, TU2 had 194, and TU3 had 214 out of 1,096 days. Despite this frequency, the absence of landslides on Green or Yellow days indicates that the σ thresholds effectively minimised false alarms while maintaining high sensitivity to actual landslide occurrences.

A practical example of the system's real-time operation was observed on July 8, 2022 (Figure 5(b) and 5(c)). Initially, the SU containing the landslide was under a Green Alert, as shown in the static susceptibility map. However, as rainfall conditions evolved, the dynamic susceptibility map indicated an increased alert level raised to Orange just before the landslide occurred. This highlights the system's ability to adapt promptly to changing conditions, providing timely warnings for the affected areas.

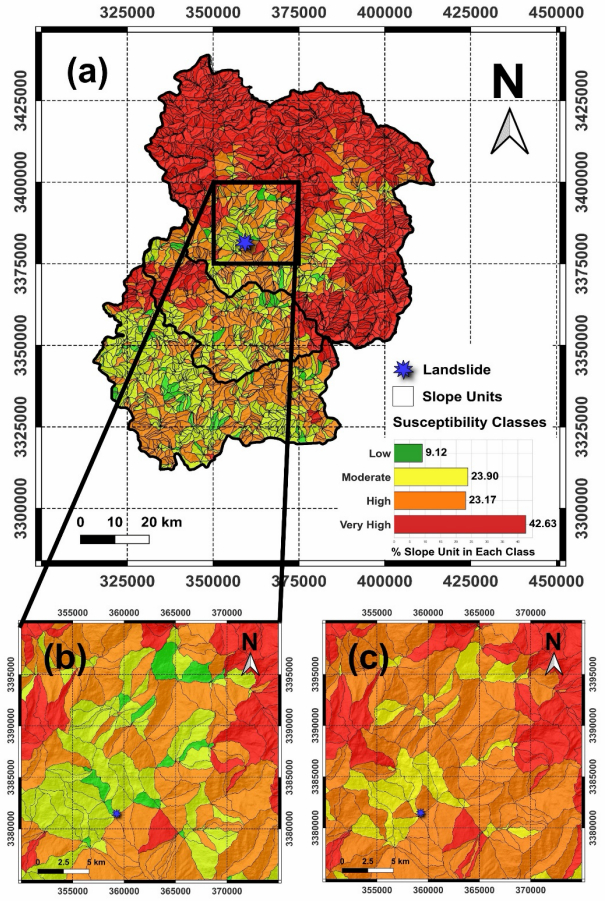

Figure 5. Summary of the Dynamic Landslide Early Warning System: (a) Static susceptibility map based on slope units (SUs); (b) Detailed view of an area displaying the static susceptibility map with the landslide site (blue star) marked on a SU under a "Green Alert"; (c) Dynamic susceptibility map for the same area on July 8, 2022, indicating an increased alert level to "Orange Alert" on the SU where the landslide took place.

5 DISCUSSION

This integrated dynamic early warning system combines SU susceptibility maps with σ rainfall thresholds to overcome the temporal limitations of static hazard maps, which identify vulnerable slopes but cannot capture immediate triggers like rainfall. By dynamically updating alerts based on real-time rainfall exceeding locally calibrated thresholds, the system monitors not only highly susceptible areas but also low and moderate susceptibility zones when conditions become critical, providing timely warnings where static maps alone cannot. Independent validation confirmed this approach's effectiveness, with 92.7% of landslides occurring during Red

alerts and none during low-level alerts, showing that susceptibility defines where landslides can happen, but rainfall triggers when they do. Unlike pixel-based maps that create fragmented, less meaningful patterns, SUs represent coherent, physically connected landforms shaped by natural drainage, allowing precise targeting of mitigation measures and monitoring instruments such as piezometers and inclinometers. This coherence enhances predictive capacity and reduces computational demands, enabling near real-time alerts. Operationally, the system minimises warning fatigue by issuing high-level alerts only for vulnerable SUs under critical rainfall, allowing efficient use of resources for evacuations, inspections, and infrastructure protection. Future improvements include making σ thresholds dynamic by integrating soil moisture data, increasing rain gauge density in critical areas, utilising higher-resolution rainfall and forecast data, and incorporating real-time ground sensor measurements to detect actual slope instability beyond rainfall proxies. Expanding triggers to include seismic or snowmelt events and regularly updating susceptibility maps with new landslide and land-use data will further refine accuracy. Employing ensemble modelling and clearly communicating uncertainties can also strengthen the system's reliability, making it a robust and practical tool for effective, timely landslide risk management.

6 CONCLUSION

This research advances landslide monitoring by developing and validating an integrated dynamic early warning system that bridges the gap between static susceptibility maps and real-time hazard alerts. Traditionally, susceptibility maps show where landslides may occur, but not when conditions become hazardous. By combining a high-accuracy RF model based on SUs with locally calibrated σ rainfall thresholds, this system transforms spatial hazard assessment into timely, location-specific forecasting. Independent validation confirmed that 92.7% of landslides happened during Red alerts, with none during Green or Yellow, demonstrating that susceptibility defines where landslides can occur, while rainfall thresholds determine when. Using SUs as the mapping unit offers geomorphologically meaningful, coherent spatial zones that improve planning and alert generation compared to fragmented pixel-based approaches. The system achieved perfect landslide detection (100% sensitivity) during validation and flawless reliability in stable periods (100% Negative Predictive Power), allowing decision-makers to trust no-alert conditions while minimising unnecessary disruption through spatially focused warnings. Overall, this work provides a scientifically sound, operationally practical framework that converts static hazard data into a dynamic early warning tool, representing a significant step forward in landslide risk management for mountainous, rainfall-prone areas.

7 REFERENCES

Abraham, M.T., Satyam, N., Bulzinetti, M.A., Pradhan, B., Pham, B.T. and Segoni, S., 2020a. Using Field-Based Monitoring to Enhance the Performance of Rainfall Thresholds for Landslide Warning. *Water*, [online] 12(12), p.3453. https://doi.org/10.3390/w12123453.

Abraham, M.T., Satyam, N., Pradhan, B. and Alamri, A.M., 2020b. IoT-Based Geotechnical Monitoring of Unstable Slopes for Landslide Early Warning in the Darjeeling Himalayas. *Sensors*, [online] 20(9), p.2611. https://doi.org/10.3390/s20092611.

Abraham, M.T., Satyam, N., Shreyas, N., Pradhan, B., Segoni, S., Abdul Maulud, K.N. and Alamri, A.M., 2021. Forecasting landslides using SIGMA model: a case study from Idukki, India. *Geomatics, Natural Hazards and Risk*, [online] 12(1), pp.540–559. https://doi.org/10.1080/19475705.2021.1884610.

ALOSPALSAR, 2015. *Dataset: ASF DAAC 2015, ALOS PALSAR_Radiometric_Terrain_Corrected_high_res; Includes Material © JAXA/METI 2007. Accessed through ASF DAAC 12 December 2021.* https://doi.org/https://doi.org/https://doi.org/10.5067/Z97HFCNKR6VA.

Alvioli, M., Marchesini, I., Reichenbach, P., Rossi, M., Ardizzone, F., Fiorucci, F. and Guzzetti, F., 2016. Automatic delineation of geomorphological slope units with r.slopeunits v1.0 and their optimization for landslide susceptibility modeling. *Geoscientific Model Development*, 9(11), pp.3975–3991. https://doi.org/10.5194/gmd-9-3975-2016.

Baum, R.L., Savage, W.Z. and Godt, J.W., 2008. *TRIGRS—A Fortran Program for Transient Rainfall Infiltration and Grid-Based Regional Slope-Stability Analysis, Version 2.0*.

Froude, M.J. and Petley, D.N., 2018. Global fatal landslide occurrence from 2004 to 2016. *Natural Hazards and Earth System Sciences*, [online] 18(8), pp.2161–2181. https://doi.org/10.5194/nhess-18-2161-2018.

GSI, 2024. *Bhukosh-the spatial data portal and a geophysical data repository. https://bhukosh.gsi.gov.in/Bhukosh/Public. Accessed 6 December 2024*. Available at: https://bhukosh.gsi.gov.in/Bhukosh/Public.

Gupta, K. and Satyam, N., 2022. Estimation of Arias intensity and peak ground acceleration (PGA) using probabilistic seismic hazard assessment of Uttarakhand state (India). *Arabian Journal of Geosciences*, [online] 15(5), p.437. https://doi.org/10.1007/s12517-022-09733-9.

Haque, U., da Silva, P.F., Devoli, G., Pilz, J., Zhao, B., Khaloua, A., Wilopo, W., Andersen, P., Lu, P., Lee, J., Yamamoto, T., Keellings, D., Wu, J.-H. and Glass, G.E., 2019. The human cost of global warming: Deadly landslides and their triggers (1995–2014). *Science of The Total Environment*, [online] 682, pp.673–684. https://doi.org/10.1016/j.scitotenv.2019.03.415.

IMD, 2025. *India Meteorological Department*. [online] Available at: <https://mausam.imd.gov.in/>.

Lagomarsino, D., Segoni, S., Rosi, A., Rossi, G., Battistini, A., Catani, F. and Casagli, N., 2015. Quantitative comparison between two different methodologies to define rainfall thresholds for landslide forecasting. *Natural Hazards and Earth System Sciences*, [online] 15(10), pp.2413–2423. https://doi.org/10.5194/nhess-15-2413-2015.

Martelloni, G., Segoni, S., Fanti, R. and Catani, F., 2012. Rainfall thresholds for the forecasting of landslide occurrence at regional scale. *Landslides*, [online] 9(4), pp.485–495. https://doi.org/10.1007/s10346-011-0308-2.

Mittal, A., Gupta, K. and Satyam, N., 2024. Landslide Susceptibility Mapping of Chamoli (Uttarakhand) Using Random Forest Machine Learning Method. [online] pp.207–217. https://doi.org/10.1007/978-981-99-9223-2_18.

Petley, D., 2012. Global patterns of loss of life from landslides. *Geology*, [online] 40(10), pp.927–930. https://doi.org/10.1130/G33217.1.

Reichenbach, P., Rossi, M., Malamud, B.D., Mihir, M. and Guzzetti, F., 2018. A review of statistically-based landslide susceptibility models. *Earth-Science Reviews*, [online] 180, pp.60–91. https://doi.org/10.1016/j.earscirev.2018.03.001.

Segoni, S., Tofani, V., Rosi, A., Catani, F. and Casagli, N., 2018. Combination of Rainfall Thresholds and Susceptibility Maps for Dynamic Landslide Hazard Assessment at Regional Scale. *Frontiers in Earth Science*, [online] 6. https://doi.org/10.3389/feart.2018.00085.

Vishwakarma, B.D., Ramsankaran, R., Azam, M.F., Bolch, T., Mandal, A., Srivastava, S., Kumar, P., Sahu, R., Navinkumar, P.J., Tanniru, S.R., Javed, A., Soheb, M., Dimri, A.P., Yadav, M., Devaraju, B., Chinnasamy, P., Reddy, M.J., Murugesan, G.P., Arora, M., Jain, S.K., Ojha, C.S.P., Harrison, S. and Bamber, J., 2022. Challenges in Understanding the Variability of the Cryosphere in the Himalaya and Its Impact on Regional Water Resources. *Frontiers in Water*, [online] 4. https://doi.org/10.3389/frwa.2022.909246.

Wester, P., Singh Rathore, B.M., Vasily, L.A., Sharma, E. and Molden, D., 2020. The Hindu Kush Himalaya Call to Action: Sustaining Mountain Environments and Improving Livelihoods. *Mountain Research and Development*, [online] 40(1). https://doi.org/10.1659/MRD-JOURNAL-D-20-00040.1.